



Interfacial coupling effects in g-C₃N₄/SrTiO₃ nanocomposites with enhanced H₂ evolution under visible light irradiation



Yidan Luo^{a,b}, Biao Deng^{a,b}, Yu Pu^{a,b}, Annai Liu^{a,b}, Jiaming Wang^{a,b}, Kaili Ma^{a,b}, Fei Gao^{b,c}, Bin Gao^d, Weixin Zou^{a,b,*}, Lin Dong^{a,b,*}

^a Key Laboratory of Mesoscopic Chemistry of MOE, School of Chemistry and Chemical Engineering, Nanjing University, Nanjing 210093, PR China

^b Jiangsu Key Laboratory of Vehicle Emissions Control, Center of Modern Analysis, Nanjing University, Nanjing 210093, PR China

^c School of the Environmental, Nanjing University, Nanjing 210093, PR China

^d Department of Agricultural and Biological Engineering, University of Florida, Gainesville, FL, 32611, United States

ARTICLE INFO

Keywords:

g-C₃N₄
SrTiO₃
H₂ evolution
Visible light
Built-in electric field

ABSTRACT

The g-C₃N₄/SrTiO₃ nanocomposite is an important material in photocatalysis, but little attention has been paid to their interfacial interaction in photocatalytic reaction. Herein, we prepare the g-C₃N₄/SrTiO₃ nanocomposites via a two-step mechanically milling and calcination process. The composite exhibited the highest H₂ evolution activity superior to that of the pure g-C₃N₄ and SrTiO₃ in the visible light. The results of UV-vis DRS, PL and photoelectrochemical measurements demonstrated that g-C₃N₄/SrTiO₃ exhibited more visible light adsorption and faster photo-generated charge transfer. Furthermore, the interfacial electronic structures of g-C₃N₄/SrTiO₃ nanocomposites were thoroughly characterized. According to the XPS and DFT results, with the help of a strong built-in electric field presenting in the g-C₃N₄/SrTiO₃ interface, the photo-generated electrons flow to the SrTiO₃ from g-C₃N₄, leading to the highly-efficient electron separation and more H₂O molecules photo-reduction to H₂. This work explicates the significant role of built-in electric field in H₂ evolution on g-C₃N₄/SrTiO₃ photocatalyst.

1. Introduction

With the limitations of the fossil fuel and the increasing CO₂ emissions, finding the clean, renewable and carbon-neutral alternative energy sources is urgently needed to satisfy growing energy demand. The photocatalytic H₂ evolution from water splitting with the use of solar energy is considered as a promising way, because of no destructive by-products generation and environmental friendliness. Therefore, photocatalysis technology is believed as a potential method in the face of our energy and environmental challenges in the near future. Wide bandgap semiconductors such as TiO₂, ZnO, etc. [1–5] have been explored a great deal, but their main issue is that the photocatalytic response is mainly initiated in the near-UV or UV region. Therefore, developing visible-light-driven photocatalysts is an efficient approach.

Recently, many visible-light-driven semiconductor photocatalysts have been investigated [6,7]. Among them, graphitic carbon nitride (g-C₃N₄) has attracted a lot of attention due to its good photoactivity, chemical stability, narrow band gap, and low cost [8–10]. The g-C₃N₄ is composed of 2D sheets with tri-s-triazine subunits connected through planar tertiary amino groups in a layer. Importantly, g-C₃N₄ possesses a

band gap of ca. 2.7 eV, which enables it to be a visible-light-active photocatalyst for photochemical reactions and solar energy conversion [11], such as water splitting [12,13], organic pollutant mineralization [14], and CO₂ conversion. [15] Nevertheless, single g-C₃N₄ is still far from ready to be used in real application due to its high recombination rate of photo-generated electron-hole pairs [16]. Many efforts have been employed to enhance the photocatalytic activity of g-C₃N₄, such as metal/nonmetal doping [17,18], nanostructuring [19], and coupling it with other materials [20]. As one of the effective strategies to enhance the separation and transportation of photo-generated electron-hole pairs, coupling with another semiconductor has been reported. Zhao et al. successfully prepared CdMoO₄/g-C₃N₄ composites [21], which exhibited 4.8 times of CO₂ conversion rate higher than those of g-C₃N₄. He et al. synthesized ZnO/g-C₃N₄ photocatalyst [22], yielding 4.9 times higher than the pure g-C₃N₄ in photocatalytic CO₂ reduction. Shi et al. reported hollow-TiO₂/g-C₃N₄ composites [23], in which N-TiO₂ acts as an electron trapping site, leading to higher photocatalytic H₂ evolution. The above results indicate that coupling of semiconductors might be a suitable option to improve the photocatalytic activity of g-C₃N₄.

The SrTiO₃ photocatalyst has attracted considerable attention, due

* Corresponding authors: Key Laboratory of Mesoscopic Chemistry of MOE, School of Chemistry and Chemical Engineering, Nanjing University, Nanjing, 210093, PR China.

E-mail addresses: wxzou2016@nju.edu.com (W. Zou), donglin@nju.edu.cn (L. Dong).

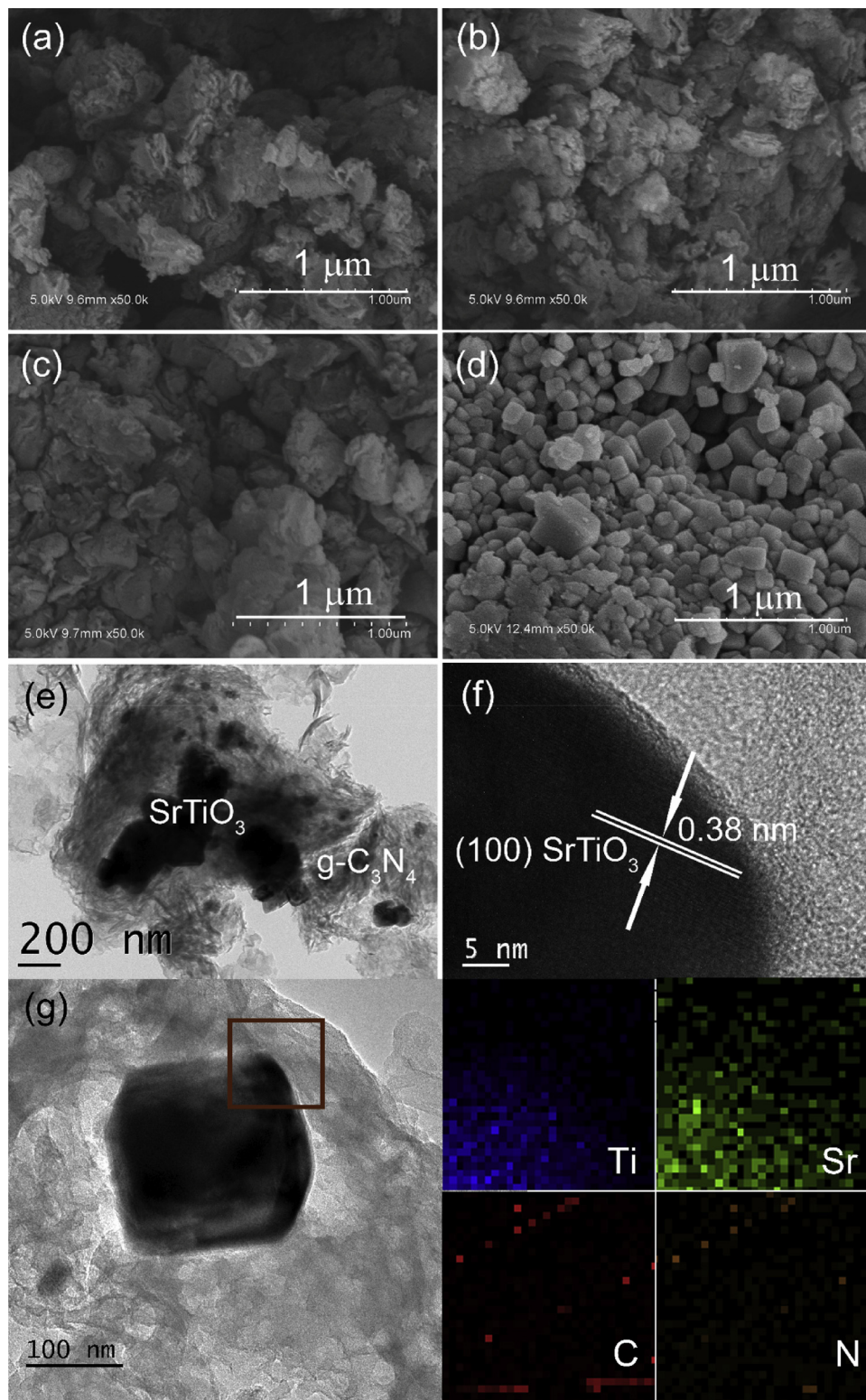


Fig. 1. SEM images of the prepared samples: (a) 3% SrTiO₃-CN, (b) 5% SrTiO₃-CN, (c) 10% SrTiO₃-CN, and (d) SrTiO₃. TEM image of (e) 5% SrTiO₃-CN and HRTEM image of (f) 5% SrTiO₃-CN. (g) HAADF-STEM-EDS elemental mapping of 5% SrTiO₃-CN.

to its excellent optical, chemical, and electronic structural properties [24,25]. As a prominent photocatalysts for reduction reactions, Rh-doped SrTiO₃ afforded significantly high efficiency for H₂ evolution under visible light [26]. The Rh and Au on SrTiO₃ photocatalyst achieved significant enhancement and high selectivity for syngas yield from the reduction of CO₂ and H₂O mixture under visible-light

irradiation [27]. N-doped SrTiO₃ nanoparticles wrapped in g-C₃N₄ nanosheets hybrid nanocomposites exhibited an improved photocatalytic activity for pollutants degradation [28]. In addition, g-C₃N₄ coated SrTiO₃ was synthesized by decomposing urea in the presence of SrTiO₃, and it possessed a higher H₂ production rate [29]. However, the interfacial electronic effects of the g-C₃N₄/SrTiO₃ are still worthy to be

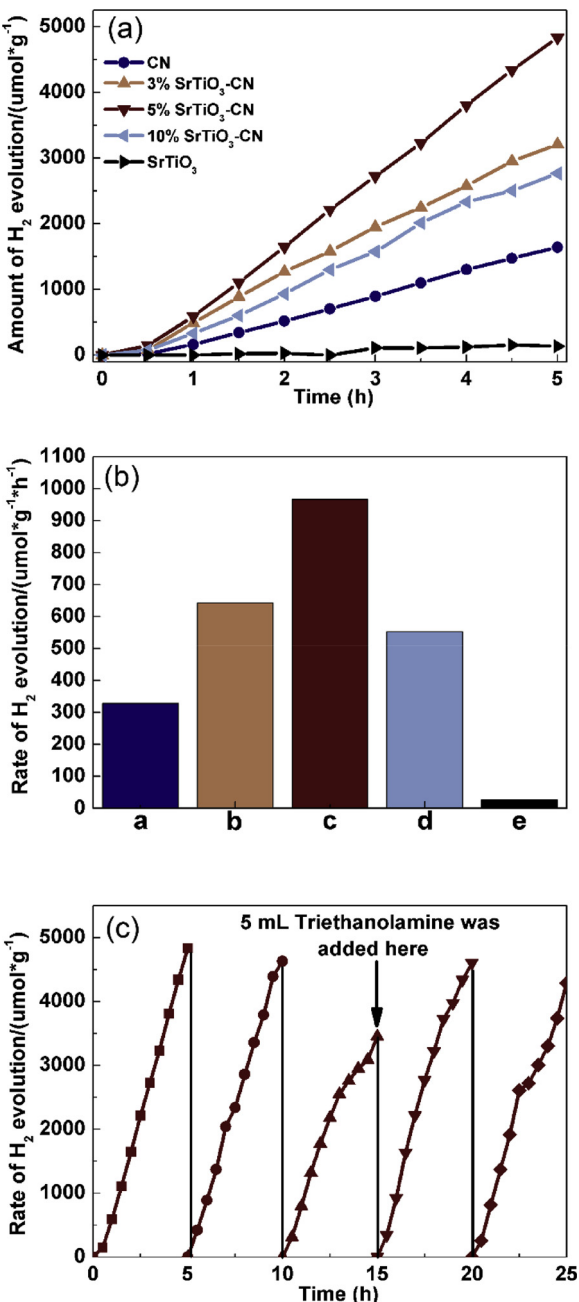


Fig. 2. (a) Time courses of photocatalytic H₂ evolution, (B) average rate of H₂ evolution over different photocatalysts, and (C) repeated time courses of photocatalytic H₂ evolution on 5% SrTiO₃-CN. The samples labeled: (a) CN, (b) 3% SrTiO₃-CN, (c) 5% SrTiO₃-CN, (d) 10% SrTiO₃-CN, (e) SrTiO₃.

investigated.

In this paper, we focused on the synergistic interaction between SrTiO₃ and g-C₃N₄ interface, and the relationships between structures, properties and photocatalytic performances were explored. The g-C₃N₄ sheets were coupled with SrTiO₃ via ball milling and subsequently calcination, and the phase structure, chemical composition, morphology and photocatalytic H₂ evolution activity of the nanocomposite were investigated in detail. Furthermore, the possible mechanisms of the enhancement of photocatalytic activity have also been provided. This work highlights the effect of interfacial coupling between g-C₃N₄ and SrTiO₃, and it would provide a new insight into the construction of stable and high efficient visible-light photocatalysts.

2. Experimental section

2.1. Synthesis of SrTiO₃/g-C₃N₄ nanocomposites

All the chemicals were of analytical grade and used without further purification. Deionized water was used in all the experiments.

The g-C₃N₄ was synthesized by calcinating urea (Aladdin) as a precursor [30]. Typically, 10 g urea was heated to 520 °C with a heating rate of 5 °C min⁻¹ and maintained at 520 °C for 2 h in a muffle furnace. The calcination process was in a covered crucible to prevent sublimation, and then the yellow powder was obtained.

In the typical synthesis of SrTiO₃, SrCO₃ (1 mmol, Aladdin), Rutile (1 mmol, Aladdin), NaCl (50 mmol, Aladdin), and KCl (50 mmol, Aladdin) were mixed and carefully ground. And the mixture was heated at 900 °C with a heating rate of 5 °C min⁻¹ and maintained at 900 °C for 5 h under static air. After cooling down to room temperature, the sample was washed with deionized water several times to remove residual salt impurity and dried in an oven at 60 °C for 24 h.

The preparation of SrTiO₃/g-C₃N₄ nanocomposites was done as follows: in brief, an appropriate amount of SrTiO₃ powder and g-C₃N₄ (0.5 g) were mixed and mechanically milled in high energy mill machine for 30 min, and then calcined at 520 °C for 2 h under static air. The hybrid nanocomposites with 3 wt%, 5 wt% and 10 wt% of SrTiO₃ are referred to as 3% SrTiO₃-CN, 5% SrTiO₃-CN, and 10% SrTiO₃-CN, respectively. As a reference, g-C₃N₄ was milled without SrTiO₃ and calcined for comparison, and the obtained product was named as CN.

2.2. Characterizations

The crystal structures were recorded by X-ray diffraction (XRD) with Philips X'Pert Pro diffractometer by Ni-filtered Cu K α radiation ($\lambda = 0.15418$ nm). Scanning electron microscopy (SEM) experiment was obtained on a Hitachi S-4800 electron microscope operated at beam energy of 10.0 kV. The catalysts were gold-coated for about 100 Å thick in a BAL-TEC SCD-500 device. Transmission electron microscopy (TEM) image was obtained on JEM-2100 instrument at an accelerating voltage of 200 kV. The samples were crushed and dispersed in A.R. grade ethanol and the resulting suspensions were dried on carbon film supported copper grids. HAADF-STEM-EDS elemental mapping analysis was performed on a double-aberration corrected Titan™ cubed G2 60–300 S/TEM equipped with Super-X™ technology. X-ray photoelectron spectroscopy (XPS) analysis was performed on PHI 5000 VersaProbe high performance electron spectrometer with an Al K α radiation (1486.6 eV) achromatic X-ray source. The samples were out-gassed at room temperature in a UHV chamber. The charging effect of samples was compensated with C 1 s peak at 284.6 eV based on the adventitious carbon. Brunauer–Emmet–Teller (BET) surface area was examined by nitrogen adsorption at 77 K on Micrometrics ASAP-2020 adsorption apparatus. Before each adsorption measurement, approximate 0.15 g catalyst was degassed in the N₂/He mixture at 90 °C for 4 h. Surface areas were estimated by using the BET method. The FT-IR spectra were measured from 400 to 4000 cm⁻¹ at the spectral resolution of 4 cm⁻¹ on Nicolet 5700 FT-IR spectrometer. The samples (5 mg) were mixed with KBr and pressed into self-supported pellets. UV-vis diffuse reflectance spectroscopy (UV-vis DRS) were recorded in the range of 200–800 nm by a Shimadzu UV-2401 spectrophotometer with the reference of BaSO₄. Photoluminescence (PL) spectra were determined on the Fluoromax-4 fluorescence spectrophotometer. The wavelength of the excitation light was 325 nm. The experiments were carried out in the solid state. The slit in all measurements was 1.5 nm. The PL spectra was measured from 350 nm to 750 nm.

2.3. Photoelectrochemical measurements

Electrochemical measurements were carried out on a CHI660 A electrochemical workstation (Shanghai Chenhua Instrument, Inc.

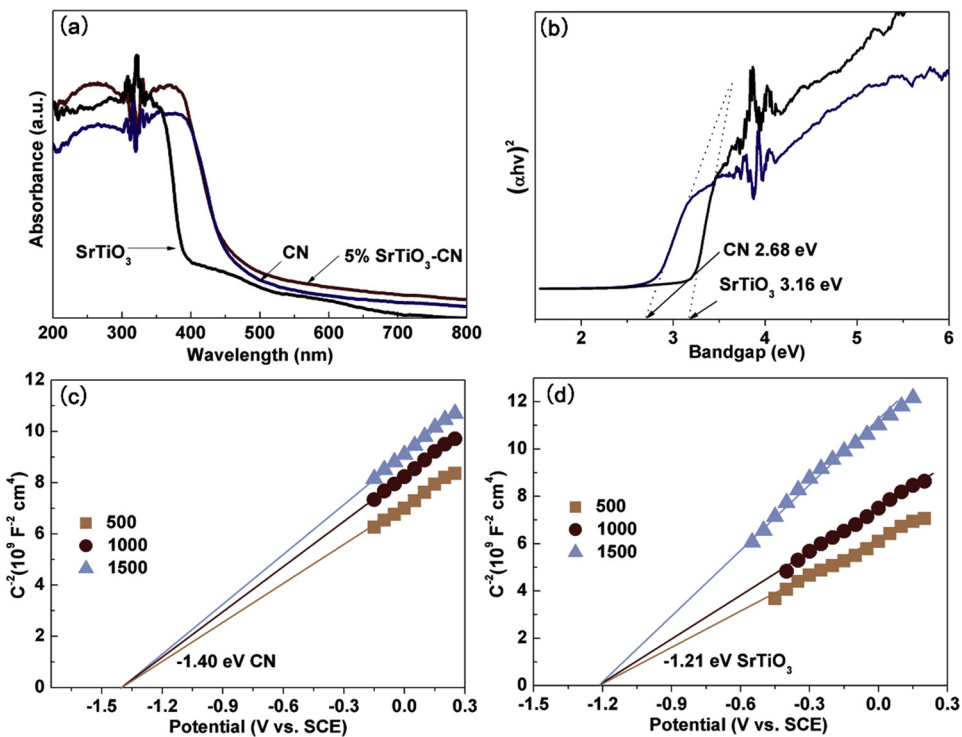


Fig. 3. (a) UV-vis absorption spectra of the CN, 5% SrTiO_3 -CN, and SrTiO_3 photocatalysts. (b) Band gap energies of CN and SrTiO_3 . Mott-Schottky plots of (c) CN and (d) SrTiO_3 at frequency 0.5 kHz, 1.0 kHz, and 1.5 kHz.

China) using a standard three-electrode cell. The prepared samples were deposited on In-doped SnO_2 -coated glass (ITO glass) electrode as the working electrodes with an active area of ca. 1 cm^2 , with a Pt wire as the counter electrode, saturated calomel electrode (SCE) as a reference electrode, and 0.5 M Na_2SO_4 aqueous solution as electrolyte. A 300 W Xe lamp with the 420 nm cut-off filter served as a light source. The working electrodes were prepared as follows: 2 mg photocatalyst was grounded with 5 mL ethanol and 10 μL 5% Nafion (DuPont) to make a slurry. Afterwards, the slurry was coated onto a $1 \text{ cm}^*1.5 \text{ cm}$ ITO glass electrode. After air-drying, the working electrode was further dried at 393 K for 2 h to improve adhesion. Finally, a homogeneous film can be obtained. The transient photocurrent densities of the as-prepared electrodes were tested at 0.5 V versus saturated calomel electrode under visible light irradiation. The Mott-Schottky curves were taken under dark with a voltage of 5 mV at a frequency of 1.5, 1.0, and 0.5 kHz. The potential ranged from -1.5 to 1.0 V (vs. SCE).

2.4. Photocatalytic H_2 generation testing

The photocatalytic hydrogen evolution reactions were carried out in a top-irradiation type vessel linked to a gas-closed glass system Ceaulight CEL-SPH2N-D (Ceaulight, Beijing, China) under an irradiation of 300 W Xe lamp with the 420 nm cut-off filter. The light intensity was 467 mW. 50 mg catalyst was dispersed in 100 mL aqueous solution containing triethanolamine (10 vol%) as a sacrificial electron donor. The H_2PtCl_6 (398 μL , 10 g/L) aqueous solution was added and then was in-situ reduced to Pt (3 wt% Pt) cocatalyst during the reaction. The temperature of the solution was kept at 6 °C. The reaction system was sealed and evacuated for 30 min before illumination. The amount of generated hydrogen was determined online by a gas chromatograph equipped with a thermal conductive detector (TCD). Argon was used as the carrier gas of the gas chromatography.

2.5. Calculation method and model

The Vienna Ab Initio Simulation Package (VASP) [31,32] for all the

spin-polarized DFT calculations within the generalized gradient approximation (GGA) using the PBE functional formulation were used in this work [33]. Projected augmented wave (PAW) pseudopotentials was employed to describe the interactions between ionic cores and valence electrons. 4 (C), 5 (N), 6 (O), 4 (Ti) and 10 (Sr) valence electrons were explicitly taken into account [34]. The valence electronic states were expanded in plane wave basis sets with a cutoff energy of 450 eV. The DFT-D3(BJ) method was used to describe the dispersion effects in the system [35]. Partial occupancies of electronic bands were allowed with the Gaussian smearing method and a width of $0.01 \text{ eV A } p(1 \times \sqrt{2})$ supercell with a single-layered corrugated $\text{g-C}_3\text{N}_4$ sheet and A $p(2 \times 3)$ supercell with six atomic-layered $\text{SrTiO}_3(001)$ were used, and the vacuum between slabs was 25 Å, in which a Monkhorst-Pack K-point mesh of $4 \times 3 \times 1$ was included.

3. Results and discussion

3.1. Crystal structure, morphology and texture properties

The crystal structure, morphology and texture properties of the as-prepared $\text{SrTiO}_3/\text{g-C}_3\text{N}_4$ nanocomposites were determined by a series of characterization methods. The XRD patterns of CN, SrTiO_3 -CN, and SrTiO_3 samples are shown in Fig. S1. The XRD patterns of CN showed two peaks at $2\theta = 13.1^\circ$ and 27.5° , which are corresponded to the (100) and (002) planes of $\text{g-C}_3\text{N}_4$, respectively. The (100) plane with the average interlayer distance ($d = 0.675 \text{ nm}$) belongs to the in-plane repeating units of the heptazine heteroatom cycles, and the (002) plane with $d = 0.324 \text{ nm}$ is related to the graphitic layer stacking, similar to graphite [11,36]. The cubic tausonite SrTiO_3 (JCPDS No. 35-0734) was identified in the pristine SrTiO_3 and SrTiO_3 -CN samples, and the peak intensity of SrTiO_3 gradually increased with the SrTiO_3 content. It was found that the position of SrTiO_3 characteristic diffraction peaks in SrTiO_3 -CN samples remained the same as those in pristine SrTiO_3 , which indicated that the introduction of $\text{g-C}_3\text{N}_4$ did not destroy the crystal structure of SrTiO_3 in all SrTiO_3 -CN samples.

FT-IR spectra of CN, SrTiO_3 , and SrTiO_3 -CN composites were

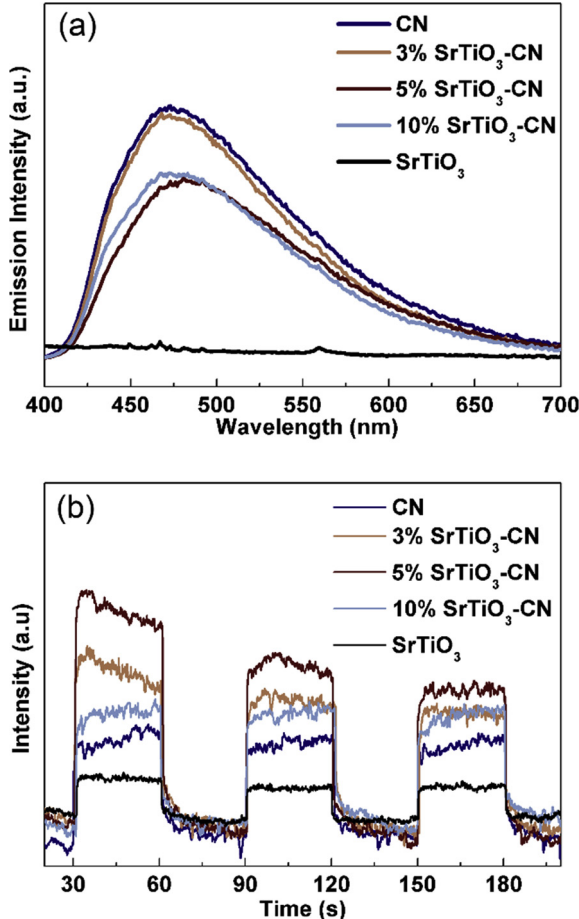


Fig. 4. (a) Room temperature PL spectra under the excitation wavelength of 325 nm and (b) Transient photocurrent response of CN, 3% SrTiO₃-CN, 5% SrTiO₃-CN, 10% SrTiO₃-CN, and SrTiO₃ photocatalysts.

presented in Fig. S2. For CN sample, the broad peak between 3600 and 2900 cm⁻¹ is related to the stretching vibration modes of the N–H and O–H stretches of the adsorbed H₂O. The prominent peaks at 1237, 1319, 1414, 1572, and 1638 cm⁻¹ correspond to typical stretching vibration modes of C=N and C–N heterocycles. [37] The peak at 809 cm⁻¹ is assigned to the out-of-plane bending vibration of the s-triazine ring. For the pristine SrTiO₃ sample, the peak at about 600 cm⁻¹ is assigned as the characteristic peak TiO₆ of SrTiO₃ [38]. Furthermore, when the SrTiO₃ are coupled with g-C₃N₄, the vibration peak attributed to SrTiO₃ weaken and broaden, which indicated that the interaction of SrTiO₃-CN on the interface was present.

The morphology and microstructure of CN, SrTiO₃-CN, and SrTiO₃ photocatalysts were characterized by SEM. As shown in Fig. S3, the accumulated layered structure of CN was observed, owing to the planar graphitic-like structure. The pristine SrTiO₃ sample shows cubic morphology (Fig. 1d). After combining with g-C₃N₄ (Fig. 1a–c), the SrTiO₃ nanoparticles are covered by g-C₃N₄. Fig. 1e and f show the transmission electron microscopy (TEM) images of 5% SrTiO₃-CN. A lattice spacing of 0.38 nm in Fig. 1f corresponding to the (001) crystal facet of SrTiO₃ (No. 35-0734) is clearly observed in 5% SrTiO₃-CN, in accordance with the XRD result. Since the (001) facet of SrTiO₃ has the lowest energy, it is expected that SrTiO₃ nanocube was primarily exposed with (001) facets [39]. In Fig. 1e, it is observed that the soft g-C₃N₄ nanosheets completely coat the SrTiO₃ particles. The HAADF-STEM-EDS elemental mapping images of Sr, Ti, C, and N in Fig. 1g further confirm the good coating of g-C₃N₄ on the surface of SrTiO₃ in SrTiO₃-CN heterostructure. The tight coupling is favorable for the charge transfer between g-C₃N₄ and SrTiO₃. Thus, we can conclude that the interface structure was mainly constructed by the SrTiO₃ (001) facets and g-C₃N₄.

In order to characterize the specific surface area and pores properties of the as-prepared CN, SrTiO₃-CN, and SrTiO₃ photocatalysts, we carried out the N₂ adsorption analysis. The nitrogen adsorption-desorption isotherms (Fig. S4a) and Barret–Joyner–Halenda (BJH) pores size distribution curves (Fig. S4b) of CN, SrTiO₃ and SrTiO₃-CN samples reveal that the all samples exhibit type IV isotherms with distinct H3 hysteresis loops, which are characteristics of mesoporous materials

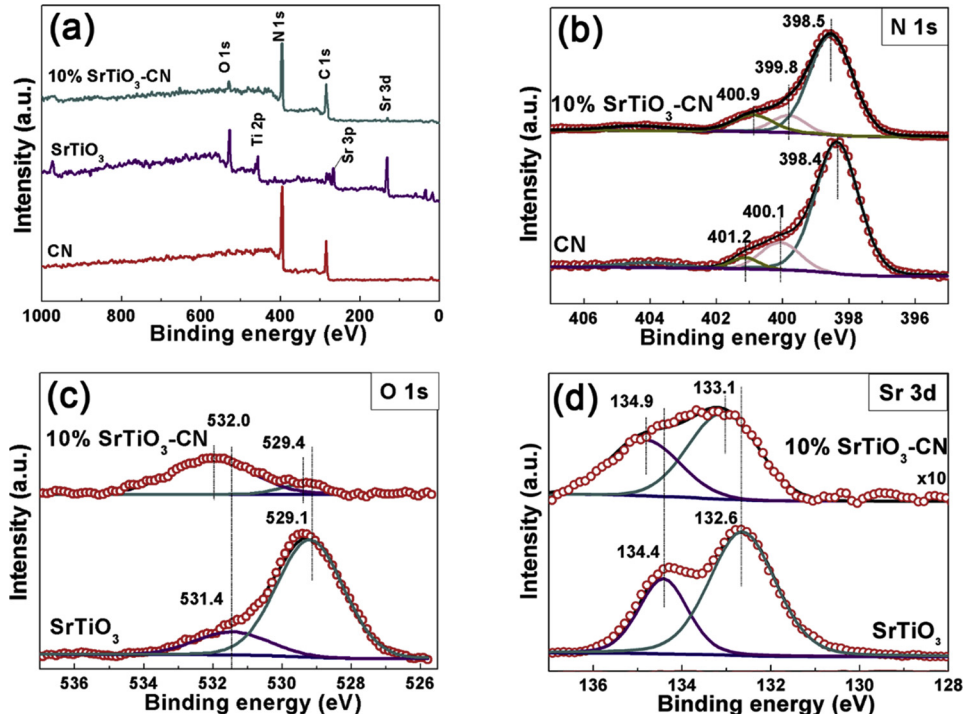


Fig. 5. (a) XPS survey spectrum of CN, 10% SrTiO₃-CN, and SrTiO₃. High-resolution XPS spectra of prepared samples: (b) N 1s, (c) O 1s, (d) Sr 3d.

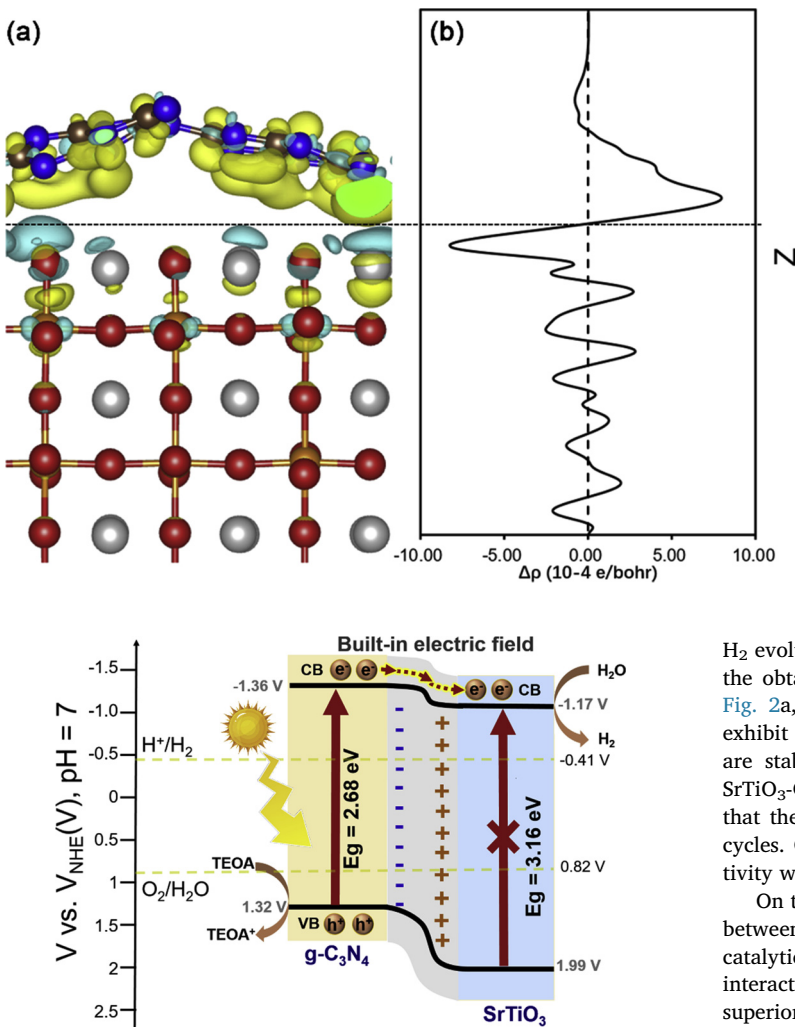


Fig. 6. (a) The isosurface map of charge density differences for g-C₃N₄/SrTiO₃, the isosurface value is 0.001 e/Å³. The cyan and yellow regions represent the electron depletion and accumulation, respectively. The C, N, O, Ti and Sr atoms are represented as brown, blue, red, yellow and sliver, respectively. (b) Planar averaged charge density difference as a function of fractional position in the Z-direction (For interpretation of the references to colour in this figure legend, the reader is referred to the web version of this article).

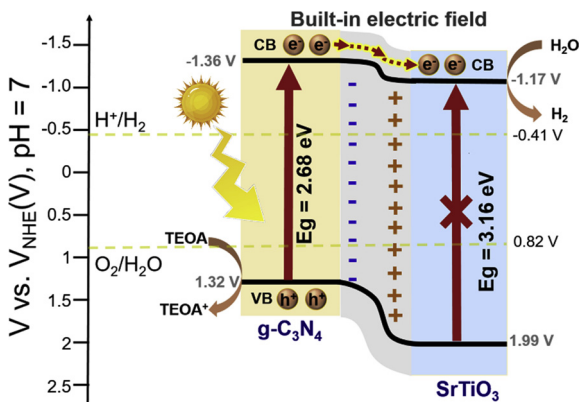


Fig. 7. Proposed mechanism for enhanced photocatalytic H₂ evolution in SrTiO₃-CN composites.

[40,41]. CN and SrTiO₃-CN samples show almost the same adsorption-desorption isotherms and pore size distribution curves. In addition, the Brunauer-Emmett-Teller (BET) specific surface areas of CN, 3% SrTiO₃-CN, 5% SrTiO₃-CN, 10% SrTiO₃-CN, and SrTiO₃ samples are calculated to be 31.9, 32.4, 30.9, 29.4, and 6.4 m²/g, respectively. As we all know, the high surface area can provide more active sites and make the composites photocatalytic process more efficient. Thus, the results of pore size and specific surface area reveal that surface area may not be the main reason for the enhanced photocatalytic activity of SrTiO₃-CN composites.

3.2. Photocatalytic H₂ evolution

The photocatalytic activity of the prepared samples toward water splitting was evaluated in the presence of 10 vol% triethanolamine (TEOA) as a sacrificial agent and 3 wt% platinum as a co-catalyst under visible light irradiation. The average photocatalytic H₂-evolution rates over various photocatalysts are displayed in Fig. 2b in comparison. The SrTiO₃ shows the lowest H₂-generation activity for its low visible-light absorption, and other H₂-evolution rates were measured to be 641.8, 966.8, 553.4, and 328.4 μmol g⁻¹ h⁻¹ for 3%, 5%, 10% SrTiO₃-CN, and CN, respectively. The results demonstrate that although the photocatalytic performance of SrTiO₃ is poor and the combination of SrTiO₃ is beneficial for the enhanced activity compared to the pure CN. Furthermore, the 5% SrTiO₃-CN sample exhibited the superior activity for

H₂ evolution than other SrTiO₃-CN samples. Moreover, the stability of the obtained catalysts in the reaction is determined. As observed in Fig. 2a, the rates of hydrogen evolution over the prepared samples exhibit a linear increase in the reactions, implying that photocatalysts are stable under light illumination. The photocatalytic test of 5% SrTiO₃-CN in 5 cycles was further carried out (Fig. 2c), it demonstrated that the hydrogen evolution activity was unchanged in the first two cycles. Once TEOA was added in the reaction, the photocatalytic activity was recovered. Thus, the 5% SrTiO₃-CN has good photostability.

On the basis of the above results, it was deduced that the interface between SrTiO₃ and CN would play a key role in the enhanced photocatalytic performance, and thus the relationships between interfacial interaction and chemical properties are explored in detail. Generally, superior H₂ evolution performance was mainly attributed to the large surface area, available visible light absorption, and highly-effective charge separation. From the results of surface area, it is concluded that the specific surface area may not be the reason for the enhanced photocatalytic activity of SrTiO₃-CN.

3.3. Optical and photoelectrochemical properties

The optical absorption properties of the as-synthesized samples were studied by UV-vis diffuse reflectance spectroscopy. As observed in Fig. 3a, CN absorbs the light from UV to visible region at 460 nm, owing to the charge transfer from the valence band (VB) to the conduction band (CB). Whereas, SrTiO₃ can only absorb the light with $\lambda < 390$ nm, due to its wide band gap. However, in the present of CN, more visible light is absorbed by SrTiO₃-CN. The band gap values (E_g) of the samples are determined by the tangent lines of $(ahv)^2$ against energy (hv), as shown in Fig. 3b [42–44]. The estimated band-gap values are ca. 2.68 and 3.16 eV corresponding to CN and SrTiO₃, respectively.

In addition, the Mott-Schottky (M-S) plots are employed to determine the types of conductivity for CN and SrTiO₃ as well as their flat-band potential (E_{fb}). As shown in Fig. 3c and d, the results show that the positive slopes correspond to n-type property of CN and SrTiO₃ [45]. Moreover, the flat potentials for CN and SrTiO₃ are -1.40 and -1.21 V versus SCE, respectively. It is known that the conduction band potentials (E_{CB}) for n type semiconductor is more negative about -0.1 or -0.2 V than its flat band potential [46]. And thus, the E_{CB} for CN and SrTiO₃ are roughly reckoned up to be -1.60 and -1.41 V versus SCE, that is -1.36 and -1.17 V vs. normal hydrogen electrode (NHE) (E_{NHE} = E_{SCE} + 0.241 V). The valence band (VB) potentials of CN and SrTiO₃

are 1.32 and 1.99 V versus NHE calculated by the equation: $E_{VB} = E_{CB} + Eg$. The above Type-II band alignment is beneficial for the proper electrons-holes transfer in the interface of the composites, and thus the photocatalytic activity is enhanced.

Photoluminescence (PL) spectra is a well-known method to explore both transfer process of the charge carrier on interface and the recombination rate involved with the photogenerated electron-hole pairs. Herein, the PL spectra are employed to reveal the recombination abilities of the SrTiO₃-CN composites. Fig. 4a presents the PL spectra of the CN, SrTiO₃-CN, and SrTiO₃ photocatalysts at an excitation wavelength of 325 nm. The PL intensity of SrTiO₃ is very low, owing to the highly crystalline, ordered cubic structure with less extrinsic defects of SrTiO₃ after calcination at 900 °C. The emission band for pristine CN was centered at 460 nm, which was attributed to the radiative recombination process of self-trapped excitations. Noteworthy, the PL intensity of the SrTiO₃-CN heterostructures decreased compared to CN, and 5% SrTiO₃-CN shows the lowest PL intensity in all composites. The fluorescence quenching via coupling SrTiO₃ mainly results from improved interfacial charge transfer between SrTiO₃ and g-C₃N₄, which could improve the separation of photo-excited electron-hole pairs, leading to the enhanced photocatalytic activity.

In addition, the transient photocurrent responses of pristine CN, SrTiO₃-CN, and SrTiO₃ photocatalysts electrodes were determined (Fig. 4b). As expected, the SrTiO₃-CN composites exhibit the higher photocurrent response than that of pristine CN and SrTiO₃, which indicates the higher separation efficiency of photogenerated carriers on the interface of the composites. With increasing the content of SrTiO₃, there is a peak value for the photocurrent intensity, and the 5% SrTiO₃-CN displays the highest photocurrent respond. The photocurrent values in 3% SrTiO₃-CN and 5% SrTiO₃-CN decrease with irradiation time, which indicates that the recombination of photogenerated electron-hole pairs occurs in the process. The photoelectrons recombine with the holes which accumulated on the surface of the samples rather than trapped by reduced species in the electrolyte, thus the photo current decays [47–49]. Based on the above results, it is suggested that the superior interfacial coupling between SrTiO₃ and g-C₃N₄ has a positive influence on visible light absorption and photo-generated electrons-holes transfer, and then enhances the photocatalytic H₂ evolution.

3.4. Interfacial interactions of SrTiO₃-CN

In order to gain further insight into the interfacial electronic structures, we use the XPS technology to investigate the surface electronic structure and bonding configuration of SrTiO₃-CN composites. The survey XPS spectra of the CN, 10% SrTiO₃-CN, and SrTiO₃ samples are shown in Fig. 5a. For the SrTiO₃-CN sample, the peaks attributed to C, N, Sr, O elements were observed in survey XPS spectra, whereas, the Ti signal was found in the high-resolution XPS spectra (Fig. S5b). In Fig. S5a, the high-resolution C 1 s spectrum in CN could be divided into two main peaks centered at ca. 284.6 and 288.0 eV. The weak peak at 284.6 eV is responsible for the adventitious carbon in g-C₃N₄, which is determined as standard carbon [50]. The strong peak at 288.0 eV was assigned to sp²-bonded carbon atoms in the heterocycle (N—C = N) of the aromatic g-C₃N₄, which is the major skeleton carbon in the triazine-based heterocycle [8]. Compared to CN sample, the binding energy of the N—C=N groups on SrTiO₃-CN was barely shifted. Furthermore, the N 1 s XPS spectra for CN and SrTiO₃-CN are displayed in Fig. 5b. The N 1 s spectrum of CN is deconvoluted to three peaks at 398.4, 400.1, and 401.2 eV. The dominant peak at 398.4 eV is assigned to sp²-hybridized nitrogen (pyridine N) in triazine rings (C—N=C). [51]. The peak at 400.1 eV corresponds to ternary nitrogen (pyrrolic N) bonded to carbon atoms in the form of N-(C)₃ [52]. The pyridine N and pyrrolic N together with N—C = N form the heptazine heterocyclic ring units, which are the main substructure of g-C₃N₄. The peak at 401.2 eV is related to the presence of amino groups (graphitic N, C-N-H) [53]. After combined with SrTiO₃, the peaks attributed to pyrrolic N [N-(C)₃] and graphitic N

(C—N-H) were shifted to the lower binding energies, indicated that the electrons from SrTiO₃ flowed into the triazine rings of CN between SrTiO₃-CN interface. The pyridine N was barely shifted on SrTiO₃-CN, which indicated a weak interaction between pyridine N and SrTiO₃. A similar phenomenon has also been reported between CoP/g-C₃N₄ [54].

In the O 1 s spectrum of SrTiO₃ (Fig. 5c), the asymmetric peak at 529.1 eV is assigned to the O²⁻ species binding energy characteristic of oxide materials. [43] The shoulder peak observed at 531.4 eV can be attributed to the chemisorbed oxygen species on surface [55]. The peak of lattice oxygen O²⁻ species (529.4) in SrTiO₃-CN exhibits a positive shift relative to that of SrTiO₃ (around 529.1 eV), as well as a positive shift of chemisorbed oxygen, suggesting that electrons on the O atoms of SrTiO₃ in composites are lost. In the fitting peaks of Sr 3d (Fig. 5d) in SrTiO₃ sample, a major peak at 132.6 eV with a shoulder at 134.4 eV are ascribed to the 3d_{5/2} and 3d_{3/2} core level of Sr²⁺ [56]. The binding energies of Sr 3d_{5/2} and Sr 3d_{3/2} of SrTiO₃-CN are located at 133.1 and 134.9 eV, which are 0.5 eV higher than in SrTiO₃ sample. Combined with the XPS results of N 1 s and C 1 s, it was suggested that electrons on O and Sr atoms (SrTiO₃) are donated to the ring of the s-triazine (g-C₃N₄) on the SrTiO₃-CN interface.

In order to further confirm the interfacial electronic interaction of the nanocomposites, the variation of electronic density of the SrTiO₃-CN nanocomposites was calculated. This can be expressed as (as shown in Fig. 6): $\Delta\rho = \rho(g\text{-C}_3\text{N}_4/\text{SrTiO}_3) - \rho(g\text{-C}_3\text{N}_4) - \rho(\text{SrTiO}_3)$, where $\rho(g\text{-C}_3\text{N}_4/\text{SrTiO}_3)$ is the electron density of the total g-C₃N₄/SrTiO₃ system, and $\rho(\text{SrTiO}_3)$ and $\rho(g\text{-C}_3\text{N}_4)$ are the unperturbed electron densities of the SrTiO₃ (001) and g-C₃N₄ sheet, respectively. In Fig. 6a, the cyan and yellow regions represent the electron depletion and accumulation, respectively. A strong regions of charge accumulation is found on the g-C₃N₄, whereas the charge depletion appears on the Sr and O atoms of SrTiO₃. Fig. 6b plots the planar averaged charge density difference along the direction perpendicular to the SrTiO₃ (001) surface. The positive and negative values represent electron accumulation and depletion, respectively. The electron accumulation on g-C₃N₄ and depletion of SrTiO₃ clearly demonstrated that the electrons transfer from the SrTiO₃ to g-C₃N₄. The electron distribution variation of g-C₃N₄ after combined with SrTiO₃ was shown in Fig. S6. The average electron accumulation of pyrrolic N and graphitic N c-N and graphitic- was much greater than pyridine N, which confirmed the XPS results. Based on the above results, the photo-generated electron will transfer from g-C₃N₄ to SrTiO₃ in composites, which is due to the built-in electric field caused by these electronic interactions at the interface [57]. The built-in electric field at the interface as a driving force for the transfer of the photo-generated electrons improved the charge separation and photocatalytic activity of H₂ evolution.

Meanwhile, the type II heterojunction between g-C₃N₄ and SrTiO₃ was illustrated in Fig. 7 [58]. According to the results of band gap energy and flat-band potential, the band structures of CN and SrTiO₃ were described. The reduction level for H₂ is positioned below the CB of CN and SrTiO₃, and the oxidation level for H₂O to O₂ is above the VB of CN and SrTiO₃. These band positions permit the transfer of electrons and holes for water splitting. It could be observed that upon visible light photoexcitation, electrons and holes are first generated in the CB and VB of g-C₃N₄ not SrTiO₃ of SrTiO₃-CN composites. The electrons excited from the surface of g-C₃N₄ can transfer to the CB of SrTiO₃ via the heterojunction interface, because of the lower CB position of SrTiO₃ and the driving force of the interfacial built-in electric field. Subsequently, the electrons flowed into the CB of SrTiO₃ can be transferred to the surface, in order to the reduction of adsorbed water molecules to hydrogen. On the other hand, photogenerated holes in the VB of CN are trapped by scavenger triethanolamine. Hence, the built-in electric field in the interface of SrTiO₃-CN composites decreases the recombination rate of photogenerated electrons and enhances visible-light harvesting, which results in superior photocatalytic activity for the SrTiO₃-CN heterojunction.

4. Conclusions

In summary, $\text{SrTiO}_3\text{-CN}$ nanocomposite photocatalysts with the contents of SrTiO_3 in the 1–10 wt% range were synthesized via mechanically milling and subsequently calcination process. Among all the prepared samples, 5% $\text{SrTiO}_3\text{-CN}$ exhibits the best photocatalytic performance than that of CN and SrTiO_3 , because of the formation of a type II heterojunction and the built-in electric field in interface. And the intensive interfacial electronic effects are beneficial for the faster photo-generated electron transfer and carrier separation, and enhanced photocatalytic H_2 evolution.

Acknowledgements

This work was financially supported from National Natural Science Foundation of China (21707066, 21677069, 21773106).

Appendix A. Supplementary data

Supplementary material related to this article can be found, in the online version, at doi:<https://doi.org/10.1016/j.apcatb.2019.01.089>.

References

- [1] L. Ling, L. Liu, Y. Feng, J. Zhu, Z. Bian, Synthesis of TiO_2 mesocrystal film with enhanced photocatalytic activity, *Chin. J. Catal.* 39 (2018) 639–645.
- [2] Y. Feng, L. Ling, J. Nie, K. Han, X. Chen, Z. Bian, H. Li, Z.L. Wang, Self-powered electrostatic filter with enhanced photocatalytic degradation of formaldehyde based on built-in triboelectric nanogenerators, *ACS Nano* 11 (2017) 12411–12418.
- [3] Y. Feng, H. Li, L. Ling, S. Yan, D. Pan, H. Ge, H. Li, Z. Bian, Enhanced photocatalytic degradation performance by fluid-induced piezoelectric field, *Environ. Sci. Technol.* 52 (2018) 7842–7848.
- [4] X. Chen, L. Liu, Y. Feng, L. Wang, Z. Bian, H. Li, Z.L. Wang, Fluid eddy induced piezo-promoted photodegradation of organic dye pollutants in wastewater on ZnO nanorod arrays/3D Ni foam, *Mater. Today* 20 (2017) 501–506.
- [5] M. Xu, Y. Chen, J. Qin, Y. Feng, W. Li, W. Chen, J. Zhu, H. Li, Z. Bian, Unveiling the role of defects on oxygen activation and photodegradation of organic pollutants, *Environ. Sci. Technol.* 52 (2018) 13879–13886.
- [6] Y. Huang, Y. Lu, Y. Lin, Y. Mao, G. Ouyang, H. Liu, S. Zhang, Y. Tong, Cerium-based hybrid nanorods for synergistic photo-thermocatalytic degradation of organic pollutants, *J. Mater. Chem. A* 6 (2018) 24740–24747.
- [7] Y. Feng, L. Ling, Y. Wang, Z. Xu, F. Cao, H. Li, Z. Bian, Engineering spherical lead zirconate titanate to explore the essence of piezo-catalysis, *Nano Energy* 40 (2017) 481–486.
- [8] W. Wang, T. An, G. Li, D. Xia, H. Zhao, J.C. Yu, P.K. Wong, Earth-abundant $\text{Ni}_2\text{P}/\text{g-C}_3\text{N}_4$ lamellar nanohybrids for enhanced photocatalytic hydrogen evolution and bacterial inactivation under visible light irradiation, *Appl. Catal. B: Environ.* 217 (2017) 570–580.
- [9] X. Bai, L. Wang, Y. Wang, W. Yao, Y. Zhu, Enhanced oxidation ability of $\text{g-C}_3\text{N}_4$ photocatalyst via C_{60} modification, *Appl. Catal. B: Environ.* 152–153 (2014) 262–270.
- [10] S. Yu, R.D. Webster, Y. Zhou, X. Yan, Ultrathin $\text{g-C}_3\text{N}_4$ nanosheets with hexagonal CuS nanoplates as a novel composite photocatalyst under solar light irradiation for H_2 production, *Catal. Sci. Technol.* 7 (2017) 2050–2056.
- [11] X. Wang, K. Maeda, A. Thomas, K. Takanabe, G. Xin, J.M. Carlsson, K. Domen, M. Antonietti, A metal-free polymeric photocatalyst for hydrogen production from water under visible light, *Nat. Mater.* 8 (2009) 76–80.
- [12] D.D. Zheng, G.G. Zhang, X.C. Wang, Integrating CdS quantum dots on hollow graphitic carbon nitride nanospheres for hydrogen evolution photocatalysis, *Appl. Catal. B: Environ.* 179 (2015) 479–488.
- [13] V.W. Lau, I. Moudrakovski, T. Botari, S. Weinberger, M.B. Mesch, V. Duppel, J. Senker, V. Blum, B.V. Lotsch, Rational design of carbon nitride photocatalysts by identification of cyanamide defects as catalytically relevant sites, *Nat. Commun.* 7 (2016) 12165.
- [14] D.M. Chen, K.W. Wang, W.Z. Hong, R.L. Zong, W.Q. Yao, Y.F. Zhu, Visible light photoactivity enhancement via CuTCPP hybridized $\text{g-C}_3\text{N}_4$ nanocomposite, *Appl. Catal. B: Environ.* 166 (2015) 366–373.
- [15] J. Zhou, W. Chen, C. Sun, L. Han, C. Qin, M. Chen, X. Wang, E. Wang, Z. Su, Oxidative polyoxometalates modified graphitic carbon nitride for visible-light CO_2 reduction, *ACS Appl. Mater. Interfaces* 9 (2017) 11689–11695.
- [16] A. Meng, S. Wu, B. Cheng, J. Yu, J. Xu, Hierarchical $\text{TiO}_2/\text{Ni(OH)}_2$ composite fibers with enhanced photocatalytic CO_2 reduction performance, *J. Mater. Chem. A* 6 (2018) 4729–4736.
- [17] Z.A. Lan, G. Zhang, X. Wang, A facile synthesis of Br-modified $\text{g-C}_3\text{N}_4$ semiconductors for photoredox water splitting, *Appl. Catal. B: Environ.* 192 (2016) 116–125.
- [18] T. Sun, H. Jiang, C. Ma, F. Mao, B. Xue, Ag/g-C₃N₄ photocatalysts: Microwave-assisted synthesis and enhanced visible-light photocatalytic activity, *Catal. Commun.* 79 (2016) 45–48.
- [19] S. Le, T. Jiang, Q. Zhao, X. Liu, Y. Li, B. Fang, M. Gong, Cu-doped mesoporous graphitic carbon nitride for enhanced visible-light driven photocatalysis, *RSC Adv.* 6 (2016) 38811–38819.
- [20] J. Wang, P. Guo, M. Dou, J. Wang, Y. Cheng, P.G. Jönsson, Z. Zhao, Visible light-driven $\text{g-C}_3\text{N}_4/\text{m-Ag}_2\text{Mo}_2\text{O}_7$ composite photocatalysts: synthesis, enhanced activity and photocatalytic mechanism, *RSC Adv.* 4 (2014) 51008–51015.
- [21] L. Zhao, L. Zhang, H. Lin, Q. Nong, M. Cui, Y. Wu, Y. He, Fabrication and characterization of hollow CdMoO_4 coupled $\text{g-C}_3\text{N}_4$ heterojunction with enhanced photocatalytic activity, *J. Hazard. Mater.* 299 (2015) 333–342.
- [22] Y. He, Y. Wang, L. Zhang, B. Teng, M. Fan, High-efficiency conversion of CO_2 to fuel over $\text{ZnO}/\text{g-C}_3\text{N}_4$ photocatalyst, *Appl. Catal. B: Environ.* 168 (2015) 1–8.
- [23] X. Shi, M. Fujitsuka, Z. Lou, P. Zhang, T. Majima, In situ nitrogen-doped hollow- $\text{TiO}_2/\text{g-C}_3\text{N}_4$ composite photocatalysts with efficient charge separation boosting water reduction under visible light, *J. Mater. Chem. A* 5 (2017) 9671–9681.
- [24] H.A. Abbas, T.S. Jamil, Nano sized Fe doped strontium titanate for photocatalytic degradation of dibutyl phthalate under visible light, *Adv. Mater. Lett.* 7 (2016) 467–471.
- [25] Y. Ham, T. Minegishi, T. Hisatomi, K. Domen, A SrTiO_3 photoanode prepared by the particle transfer method for oxygen evolution from water with high quantum efficiencies, *Chem. Commun.* 52 (2016) 5011–5014.
- [26] S. Okunaka, H. Tokudome, R. Abe, Facile water-based preparation of Rh-doped SrTiO_3 nanoparticles for efficient photocatalytic H_2 evolution under visible light irradiation, *J. Mater. Chem. A* 3 (2015) 14794–14800.
- [27] D. Li, S. Ouyang, H. Xu, D. Lu, M. Zhao, X. Zhang, J. Ye, Synergistic effect of Au and Rh on SrTiO_3 in significantly promoting visible-light-driven syngas production from CO_2 and H_2O , *Chem. Commun.* 52 (2016) 5989–5992.
- [28] S. Kumar, S. Tonda, A. Baruah, B. Kumar, V. Shanker, Synthesis of novel and stable $\text{g-C}_3\text{N}_4/\text{N-doped SrTiO}_3$ hybrid nanocomposites with improved photocurrent and photocatalytic activity under visible light irradiation, *Dalton Trans.* 43 (2014) 16105–16114.
- [29] X. Xu, G. Liu, C. Randorn, J.T.S. Irvine, $\text{g-C}_3\text{N}_4$ coated SrTiO_3 as an efficient photocatalyst for H_2 production in aqueous solution under visible light irradiation, *Int. J. Hydrogen Energy* 36 (2011) 13501–13507.
- [30] Y.W. Zhang, J.H. Liu, G. Wu, W. Chen, Porous graphitic carbon nitride synthesized via direct polymerization of urea for efficient sunlight-driven photocatalytic hydrogen production, *Nanoscale* 4 (2012) 5300–5303.
- [31] G. Kresse, J. Furthmüller, Efficient iterative schemes for ab initio total-energy calculations using a plane-wave basis set, *Phys. Rev. B* 54 (1996) 11169–11186.
- [32] G. Kresse, J. Furthmüller, Efficiency of ab-initio total energy calculations for metals and semiconductors using a plane-wave basis set, *Comp. Mater. Sci.* 6 (1996) 15–50.
- [33] J.P. Perdew, K. Burke, M. Ernzerhof, Generalized gradient approximation made simple, *Phys. Rev. Lett.* 77 (1996) 3865–3868.
- [34] G. Kresse, D. Joubert, From ultrasoft pseudopotentials to the projector augmented-wave method, *Phys. Rev. B* 59 (1999) 1758–1775.
- [35] S. Grimme, S. Ehrlich, L. Goerigk, Effect of the damping function in dispersion corrected density functional theory, *J. Comput. Chem.* 32 (2011) 1456–1465.
- [36] J. Ma, C. Wang, H. He, Enhanced photocatalytic oxidation of NO over $\text{g-C}_3\text{N}_4\text{-TiO}_2$ under UV and visible light, *Appl. Catal. B: Environ.* 184 (2016) 28–34.
- [37] K.C. Christoforidis, T. Montini, E. Bontempi, S. Zafeiratos, J.J. Delgado Jaen, P. Fornasiero, Synthesis and photocatalytic application of visible-light active $\text{Fe}_2\text{O}_3/\text{g-C}_3\text{N}_4$ hybrid nanocomposites, *Appl. Catal. B: Environ.* 187 (2016) 171–180.
- [38] H. Yu, J. Wang, S. Yan, T. Yu, Z. Zou, Elements doping to expand the light response of SrTiO_3 , *J. Photochem. Photobiol. A: Chem.* 275 (2014) 65–71.
- [39] F.A. Rabuffetti, H.-S. Kim, J.A. Enterkin, Y. Wang, C.H. Lanier, L.D. Marks, K.R. Poeppelmeier, P.C. Stair, Synthesis-dependent first-order Raman scattering in SrTiO_3 nanocubes at room temperature, *Chem. Mater.* 20 (2008) 5628–5635.
- [40] X. Yuan, C. Zhou, Y. Jin, Q. Jing, Y. Yang, X. Shen, Q. Tang, Y. Mu, A.-K. Du, Facile synthesis of 3D porous thermally exfoliated $\text{g-C}_3\text{N}_4$ nanosheet with enhanced photocatalytic degradation of organic dye, *J. Colloid Interface Sci.* 468 (2016) 211–219.
- [41] Y. Li, R. Jin, X. Fang, Y. Yang, M. Yang, X. Liu, Y. Xing, S. Song, In situ loading of Ag_2WO_4 on ultrathin $\text{g-C}_3\text{N}_4$ nanosheets with highly enhanced photocatalytic performance, *J. Hazard. Mater.* 313 (2016) 219–228.
- [42] J. Yan, Z. Chen, H. Ji, Z. Liu, X. Wang, Y. Xu, X. She, L. Huang, L. Xu, H. Xu, H. Li, Construction of a 2D graphene-like $\text{MoS}_2/\text{g-C}_3\text{N}_4$ heterojunction with enhanced visible-light photocatalytic activity and photoelectrochemical activity, *Chem. Eur. J.* 22 (2016) 4764–4773.
- [43] Y. Yao, F. Lu, Y. Zhu, F. Wei, X. Liu, C. Lian, S. Wang, Magnetic core-shell $\text{CuFe}_2\text{O}_4@\text{g-C}_3\text{N}_4$ hybrids for visible light photocatalysis of Orange II, *J. Hazard. Mater.* 297 (2015) 224–233.
- [44] G. Zhang, S. Sun, W. Jiang, X. Miao, Z. Zhao, X. Zhang, D. Qu, D. Zhang, D. Li, Z. Sun, A novel perovskite $\text{SrTiO}_3\text{-Ba}_2\text{FeNbO}_6$ solid solution for visible light photocatalytic hydrogen production, *Adv. Energy Mater.* 7 (2017) 1600932.
- [45] S. Huo, D. Qu, L. An, W. Jiang, Y. Wen, X. Wang, Z. Sun, Highly efficient p-type $\text{Cu}_3\text{P}/\text{n-type g-C}_3\text{N}_4$ photocatalyst through Z-scheme charge transfer route, *Appl. Catal. B: Environ.* 240 (2019) 253–261.
- [46] X. Hao, J. Zhou, Z. Cui, Y. Wang, Y. Wang, Z. Zou, Zn-vacancy mediated electron-hole separation in $\text{ZnS}/\text{g-C}_3\text{N}_4$ heterojunction for efficient visible-light photocatalytic hydrogen production, *Appl. Catal. B: Environ.* 229 (2018) 41–51.
- [47] X. Hao, Y. Hu, Z. Cui, J. Zhou, Y. Wang, Z. Zou, Self-constructed facet junctions on hexagonal CdS single crystals with high photoactivity and photostability for water splitting, *Appl. Catal. B: Environ.* 244 (2019) 694–703.
- [48] J. Yu, K. Wang, W. Xiao, B. Cheng, Photocatalytic reduction of CO_2 into

hydrocarbon solar fuels over g-C₃N₄-Pt nanocomposite photocatalysts, *Phys. Chem. Chem. Phys.* 16 (2014) 11492–11501.

[49] Y. Zhang, M. Xu, H. Li, H. Ge, Z. Bian, The enhanced photoreduction of Cr(VI) to Cr(III) using carbon dots coupled TiO₂ mesocrystals, *Appl. Catal. B: Environ.* 226 (2018) 213–219.

[50] W. Zou, L. Zhang, L. Liu, X. Wang, J. Sun, S. Wu, Y. Deng, C. Tang, F. Gao, L. Dong, Engineering the Cu₂O-reduced graphene oxide interface to enhance photocatalytic degradation of organic pollutants under visible light, *Appl. Catal. B: Environ.* 181 (2016) 495–503.

[51] C. Li, Y. Du, D. Wang, S. Yin, W. Tu, Z. Chen, M. Kraft, G. Chen, R. Xu, Unique P-Co-N surface bonding states constructed on g-C₃N₄ nanosheets for drastically enhanced photocatalytic activity of H₂ evolution, *Adv. Funct. Mater.* 27 (2017) 1604328.

[52] D. Zheng, G. zhang, X. Wang, Integrating CdS quantum dots on hollow graphitic carbon nitride nanospheres for hydrogen evolution photocatalysis, *Appl. Catal. B: Environ.* 179 (2015) 479–488.

[53] W. Jo, T. Adinaveen, J.J. Vijaya, N.C.S. Selvam, Synthesis of MoS₂ nanosheet supported Z-scheme TiO₂/g-C₃N₄ photocatalysts for the enhanced photocatalytic degradation of organic water pollutants, *RSC Adv.* 6 (2016) 10487–10497.

[54] H. Huang, X. Li, J. Wang, F. Dong, P.K. Chu, T. Zhang, Y. Zhang, Anionic group self-doping as a promising strategy: band-gap engineering and multi-functional applications of high-performance CO₃²⁻-doped Bi₂O₂CO₃, *ACS Catal.* 5 (2015) 4094–4103.

[55] M. Piumetti, S. Bensaid, N. Russo, D. Fino, Nanostructured ceria-based catalysts for soot combustion: investigations on the surface sensitivity, *Appl. Catal. B: Environ.* 165 (2015) 742–751.

[56] T. Kanagaraj, S. Thiripuranthagam, Photocatalytic activities of novel SrTiO₃-BiOBr heterojunction catalysts towards the degradation of reactive dyes, *Appl. Catal. B: Environ.* 207 (2017) 218–232.

[57] J. Liu, Origin of high photocatalytic efficiency in monolayer g-C₃N₄/CdS Heterostructure: a hybrid DFT study, *J. Phys. Chem. C* 119 (2015) 28417–28423.

[58] M.R. Gholipour, D. Cao-Thang, F. Beland, D. Trong-On, Nanocomposite heterojunctions as sunlight-driven photocatalysts for hydrogen production from water splitting, *Nanoscale* 7 (2015) 8187–8208.